Review of Scientific Instruments ARTICLE pubs.aip.org/aip/rsi

A superconducting transition edge sensor array for synchrotron soft x-ray emission spectroscopies of low-dimensional and impurity-level concentration systems

Cite as: Rev. Sci. Instrum. 97, 065208 (2026); doi: 10.1063/5.0332443
Submitted: 4 March 2026 • Accepted: 26 May 2026 •
Published Online: 10 June 2026

Régis Decker,[1,a] Kelsey M. Morgan,[2,3] Sergey Peredkov,[4] Charles J. Titus,[5] Galen C. O'Neil,[2] Alexander Dillmann,[6] Dmitry Tikhonov,[4] Utkarsh Prakash,[4] Axel Knop-Gericke,[4] Joseph W. Fowler,[2,3] Jonathan W. Dean,[2,3] Nathan Nakamura,[2] Raoul Blume,[4] Detre Techner,[4] Minmin Chen,[4] Zechao Jin,[1] Christian Weniger,[1] Thomas Blume,[1] Torsten Kachel,[1] Nathan J. Ortiz,[2] Douglas A. Bennett,[2] John A. B. Mates,[2] Daniel R. Schmidt,[2] Jozsef Imrek,[7] Joel C. Weber,[3] Johnathon D. Gard,[3] Leila Vale,[2] Abigail L. Wessels,[2,3] Bastian Klemke,[6] Sebastian Gerischer,[6] Mattis Fondell,[1] Sebastian Eckert,[1] Joel N. Ullom,[2] Daniel S. Swetz,[2] Serena DeBeer,[4] and Alexander Föhlisch[1,8]

AFFILIATIONS

[1] Helmholtz-Zentrum Berlin für Materialien und Energie GmbH, Institute for Methods and Instrumentation for Synchrotron Radiation Research, 12489 Berlin, Germany
[2] National Institute of Standards and Technology, Boulder, Colorado 80305, USA
[3] Department of Physics, University of Colorado, Boulder, Colorado 80309, USA
[4] Max Planck Institute for Chemical Energy Conversion, Mülheim an der Ruhr 45470, Germany
[5] National Institute of Standards and Technology, Gaithersburg, Maryland 20899, USA
[6] Helmholtz-Zentrum Berlin für Materialien und Energie GmbH, 12489 Berlin, Germany
[7] Theiss Research, La Jolla, California 92037, USA
[8] Universität Potsdam, Institut für Physik und Astronomie, Potsdam 14476, Germany

[a] **Author to whom correspondence should be addressed:** regis.decker@helmholtz-berlin.de

ABSTRACT

We present a new instrument for soft x-ray absorption and emission spectroscopy based on the latest generation of transition edge sensor array optimized for soft x-ray detection, built on microwave superconducting quantum interference device multiplexing readout, and cooled with a dilution refrigerator. Its extreme collecting efficiency enables spectroscopy measurements on dilute systems. It also enables shorter acquisition time and large energy-range spectra. We describe the design and operation of the spectrometer and characterize its performance in terms of energy resolution, photon collecting efficiency, and stability. A resolution of 0.7–1.8 eV in the energy range 260–900 eV with a high detection rate of up to 10 000 photons per second across the array is achieved with minimal performance degradation. In addition, the use of the dilution refrigerator to cool the detector results in a robust and stable energy calibration over time. The spectrometer is attached to a dedicated ultra-high vacuum sample chamber equipped with a fully motorized sample cryostat for experiments at temperatures between 10 and 300 K, multi-sample mounting, and electric field-gated devices. The spectrometer-sample chamber is installed at a beamline providing full polarization control. We demonstrate the capabilities of the setup using two representative examples of XES on extremely low-concentration systems, namely monolayer hexagonal boron nitride and the $K_3[Fe(CN)_6]$ molecular system at sub-millimolar concentration.

I. INTRODUCTION

X-ray Absorption Spectroscopy (XAS), X-ray Emission Spectroscopy (XES), and Resonant Inelastic X-ray Scattering (RIXS) are well-established element- and orbital-selective core-level spectroscopy techniques for the study of the local electronic properties of materials.[1–4]

XAS, or Near Edge X-ray Absorption Fine Spectroscopy (NEXAFS), when the incident photon energy is tuned close to an absorption edge, is a first-order optical process where one electron is excited from a core level to an unoccupied level, below the ionization threshold. The transition mostly follows the dipolar selection rule $\Delta l = \pm 1$. XAS gives information on the local electronic structure and the local environment of the absorbing atom, like the oxidation state and the local symmetry.

XES is a second-order, photon-in/photon-out process, in which the first step (photon-in) is the creation of a core-ionized state. In XES, one measures the energy of photons emitted during the second step, in which the system relaxes via radiative decay (photon-out). It provides information on the occupied density of states, bonding orbitals, metal–ligand hybridization, and even time scales of dynamic processes through the core-hole clock method.[5–8]

While XES is the general term, it commonly refers to the nonresonant process, in which the core electron is excited well above the absorption threshold into the continuum. In RIXS, the incident photon energy is tuned to an absorption resonance, creating a core-excited intermediate state. This resonant condition enhances the scattering cross section and increases the interaction between the excited electron and the valence electrons, thereby strengthening the coupling to the system. This can lead to a charge-neutral excited final state with the creation of elementary excitations like dd (on the order of 1 eV), charge transfer (a few eV), exciton (hundreds of meV to a few eV), plasmon (sub-eV to tens of eV), magnon (below 1 eV), and phonon (a few tens of meV) excitations, identified as energy loss features in RIXS spectra.[3] In practice, so-called RIXS maps can be recorded, where an emission spectrum is measured for each incident photon energy with a given energy interval and in the energy region of interest. Therefore, RIXS maps contain comprehensive spectroscopic information: partial fluorescence yield (PFY) absorption and emission spectra at and away from resonance(s). However, recording full RIXS maps often requires extended acquisition times because of the intrinsically low fluorescence yield in the soft x-ray regime. Together, XAS, XES, and RIXS provide complementary access to unoccupied states, occupied states, and low-energy excitations, respectively. Therefore, they form a powerful toolbox for investigating the electronic structure of complex materials.

So far, most soft x-ray XES and RIXS spectrometers are wavelength dispersive (WD) spectrometers, where x rays emitted from the sample are diffracted by gratings before being collected by a position sensitive detector [Fig. 1(a)]. This type of spectrometer can reach an energy resolution on the order of a few hundred or even tens of meV.[9–13] However, even for the state-of-the-art grating based RIXS spectrometers, considering the sample's low fluorescence yield on the order of tenths of a percent to a few percent in the case of light element K-edge and transition metal L-edges, the solid angle of the spectrometer, the grating efficiency, and the detector efficiency, the ratio of incident photon flux to detected photon flux is on the order of 10^{10}. To compensate for this low overall collecting efficiency, XES and RIXS techniques have needed high flux beamlines ($>10^{12}$ ph/s) and have so far been largely limited to the study of bulk or high-concentration systems.

These limitations have motivated the development of alternative detector concepts that increase collecting efficiency while maintaining useful spectral resolution. A very promising approach is the use of Transition Edge Sensors (TES),[14,15] which do not include any dispersive optical elements [Figs. 1(a) and 1(b)] and are characterized by a high collecting efficiency [Fig. 1(c)]. TES exploits the abrupt resistance variation with the temperature at the critical temperature of a superconductor (Fig. 2). Historically, TESs have been largely used for astrophysical measurements and, more generally, for applications where the source is faint or extended. To our knowledge, five TES x-ray spectrometers for XAS, XES, and RIXS have been deployed at synchrotron facilities: at APS 29-ID[16] and later moved to SSRL 13-3,[17] at SSRL 10-1,[18] at APS 1-BM-C,[19] at NSLS-II SST-1,[14] and at SPRING-8 BL37XU.[20]

Here, we describe a new state-of-the-art TES-based spectrometer installed as a permanent end station at the Berliner Elektronenspeicherring-Gesellschaft für Synchrotronstrahlung (BESSY II) synchrotron facility. The detector includes the latest generation of sensors for improved energy resolution and increased solid angle, a readout based on microwave SQUID multiplexing that enables operation at count rates up to ten times higher than those of previous TES readout technologies, and an operating temperature in the mK range achieved with a dilution refrigerator (DR) for high performance stability over hours of measurements.

After presenting the basic principle of the TES technology, we describe the characteristics of the spectrometer and of the dedicated sample chamber. The combined spectrometer-sample-chamber is installed on the relatively low photon flux (10^{11}–10^{12} ph/s), full polarization controlled elliptically polarized undulator with spherical grating monochromator UE52-SGM beamline. All characteristics of the setup are optimized for XES measurements on low-dimensional and low-concentration beam-sensitive systems. These include atomically thin materials such as van der Waals monolayers and engineered heterostructures, impurity-level systems such as Kondo impurities, gated quantum devices, and dilute molecular systems, including frozen-solution catalysts and proteins. These systems have been largely unavailable to XES and RIXS conducted with conventional WD spectrometers. The combination of large collecting efficiency, broad energy acceptance, and compatibility with ultra-high-vacuum environments therefore enables experiments that are difficult or impossible with conventional grating spectrometers. The performance of the setup and the first scientific test cases are presented.

II. TES SPECTROMETER

A. Principle of a TES

A TES is a thermometer that is used here as a microcalorimeter to measure the energy of single quanta—in the present case, x-ray photons.[21] Invented by Langley in 1878 to measure the sun's infrared radiation with a 10^{-5} K temperature uncertainty,[22,23] bolometers and

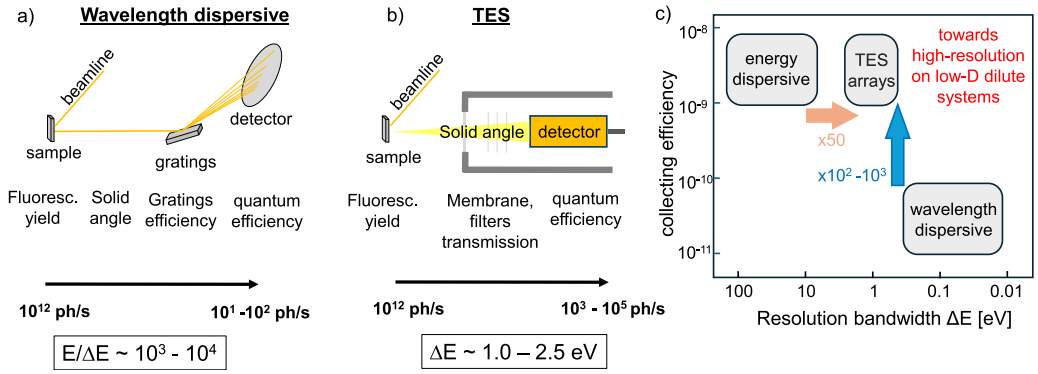

FIG. 1. Overview of common soft x-ray XES spectrometers. (a) Basic scheme of WD spectrometers. (b) Basic scheme of TES spectrometers for synchrotron applications. (c) Collecting efficiency (see text) vs resolution for the different kinds of soft x-ray photon detectors. WD spectrometers with high resolution and low collecting efficiency are primarily dedicated to bulk systems. ED spectrometers like silicon drift detectors (SDDs) and charge-coupled device (CCD) detectors have 2–3 orders of magnitude higher collecting efficiency but do not reach the energy resolution for most soft x-ray XES applications. TES spectrometers present a coarser resolution than WDs but with a collecting efficiency comparable to other EDs.

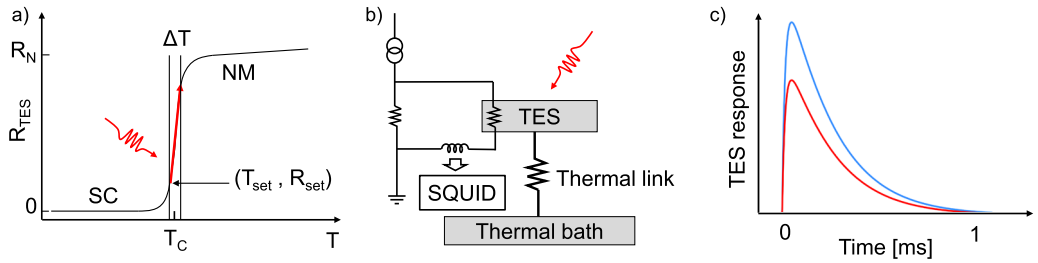

FIG. 2. Principle of a single TES for photon detection. (a) The sensor is electrically biased at the edge of the superconducting (SC) to normal metal (NM) transition at the critical temperature T_C. (b) Schematics of the TES device and electrical bias circuit. (c) Typical response of an arriving photon (blue is for a higher energy photon than red).

calorimeters consist of an absorber with heat capacity C, in thermal contact with a thermal bath of temperature T_0 and a thermometer. In the case of a TES, the thermometer is a superconducting film set at a temperature $T_0 \sim T_C$, where T_C is the critical temperature of the superconductor [Fig. 2(a)][24,25] (due to self-heating, the thermal bath [Fig. 2(b)] is set below T_C). Here, the temperature dependence of the resistance is very strong, such that the TES used here, with a heat capacity of 65 fJ/K, can distinguish μK-scale differences in the heating caused by varying energy depositions.

The basic principle of a TES is depicted in Fig. 2. In the voltage-bias mode, a voltage, U_{bias}, is applied to the TES, and the TES resistance, R_{TES}, is measured by measuring the TES current, I_{TES}.[25] An incoming photon results in a slight and fast increase of the sensor's temperature ΔT and, therefore, in an increase of the resistance ΔR, resulting in a decrease of I_{TES} through the TES. This mode is the most stable operation mode due to a sensor temperature self-regulation giving a negative electrothermal feedback, where the temperature decrease due to the decrease of I_{TES} almost compensates the photon-induced temperature increase. The combination of the negative electrothermal feedback and the thermal contact with the cryogenic bath determines the time for the TES to return to thermal equilibrium, which is on the order of ms.

The TES is connected to an inductance so that a small current variation due to an incoming photon induces a small magnetic-flux variation. A radio frequency superconducting quantum interference device (rf-SQUID) is used to measure the magnetic flux variation.

Figure 3(a) shows a single sensor. The TES thermometer (right side) is comprised of a Mo–Au bilayer, which enables us to control the critical temperature of the film. The Mo layer is patterned into two parallel 6 × 90 μm^2 long Mo wires (the long direction is parallel to the direction of the current flow), which are coated with a 30 × 90 μm^2 layer of Au, which helps to suppress the critical temperature of the film to 51 mK.[26] The entire device is suspended on a silicon nitride substrate that provides thermal isolation from the bath. The TES is in thermal contact with a 250 × 250 μm^2 large × 250 nm thick Au x-ray absorber. We refer to the combination of the TES and the x-ray absorber as a "sensor" or "pixel". The operating temperature of the sensor is 51 mK, which is an equilibrium temperature between the power dissipation due to the bias current and the power flow across the silicon nitride membrane, which

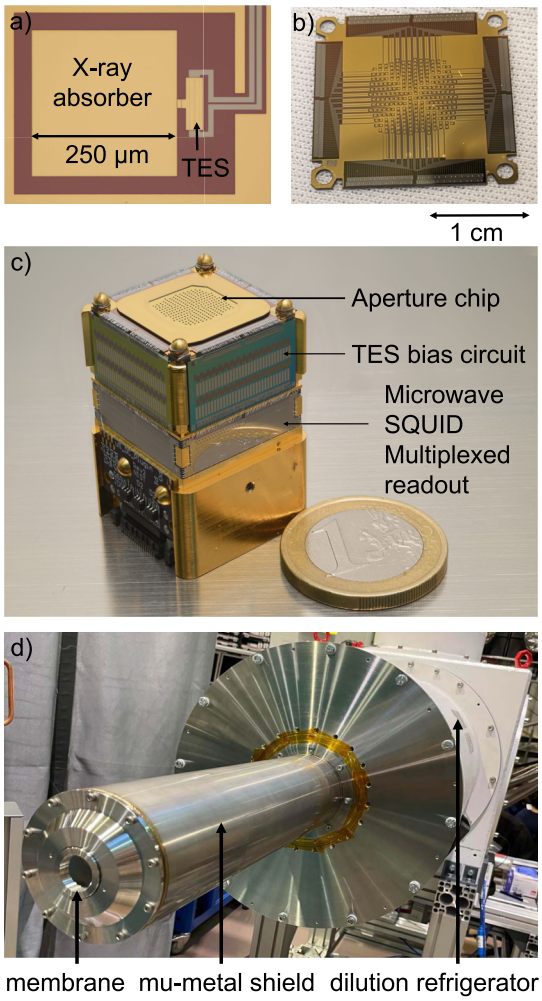

FIG. 3. TES array detector and integration in the dilution refrigerator. (a) Single sensor unit. (b) TES array chip consisting of 248 sensor units. (c) Microsnout, including the TES array chip, the aperture chip, the bias circuit, and the microwave SQUID multiplexed readout circuit in a compact geometry. (d) Final assembly of the spectrometer, including the mu-metal shielding, the filters and membrane, and the dilution refrigerator, with the microsnout being placed inside the shielding, behind the membrane.

provides the limiting thermal link to the bath temperature, set to 25 mK. The materials and geometry of the present setup are optimized for the detection of photons in the energy range 250–1000 eV, adequate for the beamline characteristics.

B. TES array

To compensate for the slow temperature decrease back to the set point and to increase the detection solid angle, the full detector comprises 248 identical pixels arranged in a 1 × 1 cm^2 array. An Au-coated silicon mask is employed to prevent photon incidence between sensors [Fig. 3(b)]. The array is located in the so-called microsnout, which also includes the bias circuit and the microwave SQUID multiplexed readout in a compact geometry [Fig. 3(c)]. In contrast to previous generations of TES detector packaging, this geometry allows upgrades to several microsnouts for an enhanced collecting efficiency. The microsnout is in thermal contact with a dilution refrigerator having a minimum base temperature of 9 mK, which allows the array to be kept at a bath temperature of 25 mK with 20 μK rms temperature stability using a PID temperature controller. Two concentric mu-metal cylinders and an aluminum housing of the microsnout ensure the thermal and magnetic shielding. To allow x-ray transmission while protecting the TES from stray optical and infrared light, the TES array is shielded by a series of three thin-film aluminum windows mounted at 25 mK, 4 K, and 40 K. These filters suppress infrared radiation and attenuate photons with energies below ~250 eV. An outer window consisting of a mesh-supported aluminum/polymer membrane separates the spectrometer's inner vacuum from that of the sample chamber. Figure 3(d) shows the completed assembly of the spectrometer.

C. Microwave SQUID multiplexing

The multiplexed readout, i.e., the use of only one or a few amplifiers shared by all sensors, aims to reduce the amount of cables at the cold stage in order to reduce both heat load and complexity. Beyond the established time domain multiplexing (TDM)[27] and frequency domain multiplexing (FDM)[28] readout technologies, the present TES array incorporates the latest generation of microwave SQUID multiplexing (μmux) to further reduce the cabling and, therefore, the heat load, and allows better scalability as well as continuous sensor monitoring. We describe here the basic principle of this approach. A detailed description of TES μmux is given by, e.g., Becker *et al.*[29] and Mates *et al.*[30]

As depicted in the μmux readout scheme [Fig. 4(a)], each TES/rf-SQUID unit is inductively coupled to a high-quality microresonator with a resonance frequency in the 4–6 GHz range, itself capacitively coupled to the feedline. Resonators have a bandwidth of 1 MHz (FWHM) with a separation of 7 MHz, which is enough to avoid cross-talk between neighboring TES/rf-SQUID/microresonator subcircuits.[31] Therefore, each subcircuit defines an independent channel for postprocessing.

The RF signal is amplified by a high electron mobility transistor (HEMT) placed at the 4 K flange of the dilution refrigerator and by a RF low-noise amplifier at the 40 K flange before it is sent to the RF in/out unit. This unit first scans the full frequency range to identify the resonance frequencies (tones) of each channel. Figure 4(b) shows the forward transmission coefficient module $|S_{21}(dB)|^2 = |\log_{10}(V_{out}/V_{in})|^2$ vs frequency. From the capacitive coupling with the feedline, each microresonator acts as a short to ground when fed with its eigenfrequency, leading to a power dissipation through the feedline. Therefore, each tone appears as a dip in the transmission spectrum. Eigenfrequencies are stable over several weeks or even months. Therefore, this procedure is typically performed only after each DR warm-up/cool-down cycle. Once the eigenfrequencies are identified, the RF in/out unit acts as a tone generator.

An incoming photon causes a change in current through the TES, which changes the flux detected by the rf-SQUID. However, an rf-SQUID response to magnetic flux is approximately sinusoidal, with a period equal to the magnetic flux quantum $\Phi_0 = h/2e \simeq 2.07 \times 10^{-15}$ Wb and is therefore degenerate and nonlinear in flux. We

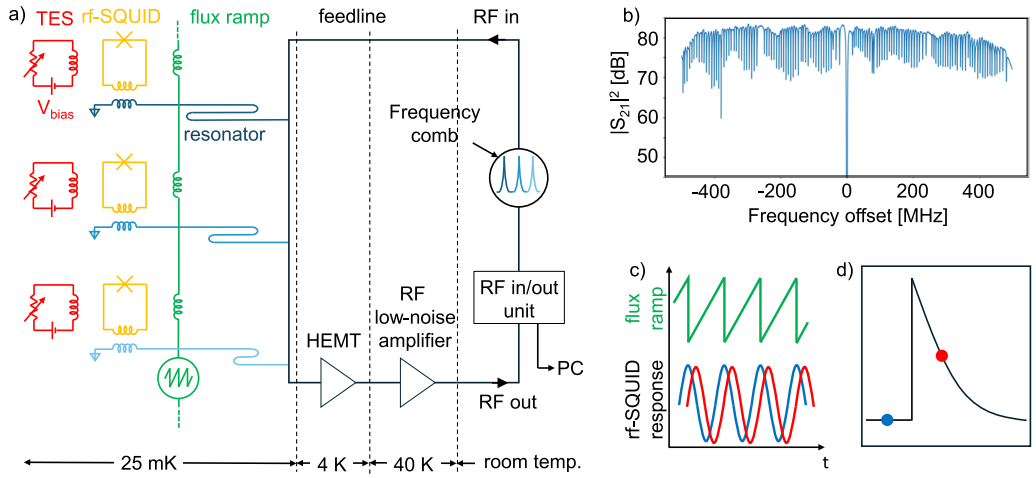

FIG. 4. Microwave SQUID multiplexing. (a) Simplified μmux readout circuit (see text).[29] (b) $|S_{21}|^2$ vs frequency response of half of the TES array. Each dip corresponds to the eigenfrequency of one resonator coupled to a sensor. (c) Sinusoidal response of an rf-SQUID (blue) to a periodic sawtooth magnetic flux (green) created by the voltage ramp [see in (a)]. The additional magnetic flux created by an incoming photon induces a phase shift in the sinusoidal response (red). (d) Illustration of a pulse with the steady state flux ramp response, before or long after an incoming photon (blue) and out-of-phase oscillation in the presence of the additional photon-originating magnetic flux (red). The pulse shape is reconstructed from the phase recording at short time intervals during a pulse duration.

use flux ramp demodulation, where each rf-SQUID is inductively coupled to a sawtooth flux ramp producing a sine oscillation of all the resonators' eigenfrequencies [Fig. 4(c)].[32] The additional magnetic flux from the TES on the rf-SQUID due to an impinging photon generates a dephasing of the periodic oscillation that is linear with flux as long as the slope of the ramp exceeds the slew rate of the input signal. The measurement of this dephasing allows the reconstruction of the pulse shape [Fig. 4(d)]. The RF multiplexing allows this operation for each channel simultaneously. It has a low heat load and low noise since it allows the simultaneous readout of all channels with a simple cabling configuration: one common voltage source for the TES bias, one common flux ramp, and one RF feedline.

D. Advantages of TES x-ray spectrometers

A TES offers four main advantages over WD XES spectrometers, which are as follows:

(1) The TESs detect photons and their energy over the whole area of the pixel, independently of the approach angle, since ΔT (and ΔR) depends on the photon energy. Therefore, a TES allows emission spectroscopy without the need for any optical element. It is, therefore, by definition, an energy dispersive photon detector.

(2) From the geometry of the TES, each photon hitting (and heating) the absorber is detected without, e.g., reflection. In addition, TESs do not have a threshold like avalanche photodiodes. These characteristics result in an extremely high quantum efficiency of 99% for photons with an energy of 700 eV and 93% for photons with an energy of 1 keV in the present instrument. This high quantum efficiency combined with the large solid angle results in a high collecting efficiency[14] $CE(E) = QE(E) \cdot T(E) \cdot \Omega \cdot N$, where QE is the quantum efficiency, T is the transmission through the outer membrane and the inner aluminum membranes,[18] Ω is the solid angle of a single TES, and N is the number of TESs in the array. During the measurements presented here, the sample-detector distance was 85 mm, corresponding to a solid angle of 8.7×10^{-6} sr per sensor and 2.1×10^{-3} sr for the full array. This corresponds to approximately two orders of magnitude larger angular acceptance than conventional grating spectrometers.[33] TES arrays typically have two to three orders of magnitude higher collecting efficiency compared to WD spectrometers [Fig. 1(c)], considering the pile-up effect discussed below.

(3) TES spectrometers have a large detection energy range, which allows the observation of features from different elements and orbitals simultaneously. The TES presented here is designed to simultaneously collect photons in the energy range of 250–1000 eV, determined by the transmission of the aluminum membranes at the low energy side and by the flux and resolution characteristics of the beamline at the high energy side. Relatively low-resolution soft x-ray WD XES spectrometers can reach a spectral energy range of 200 eV with a resolution of a few tenths of eV,[6] while the energy range of spectra shrinks to a few eV for high-resolution WD spectrometers.[34,35]

(4) Finally, a focused beam on the sample is not necessary, and a beam of a few mm^2 does not diminish the TES spectrometer's performance. It does, however, reduce the beam damage on sensitive samples.

These four main advantages make TES array spectrometers particularly adapted for low-concentration multielement beam sensitive systems. To fully exploit these capabilities for measurements on low-dimensional and dilute systems, a dedicated ultra-high-vacuum sample environment was developed and is described in Sec. III.

III. SAMPLE ENVIRONMENT

A. Sample chamber

The ultra-high vacuum (UHV) sample chamber is designed to perform XAS, XES, and RIXS experiments on the systems defined above. Specifically, the target systems include (1) low-dimensional solid state systems like impurities in solids, mono- and few layers of van der Waals materials, nanostructures, and molecules adsorbed on surfaces; and (2) millimolar concentrations of molecular systems like bioinspired molecular catalysts and proteins in frozen solutions. In the following, we describe the sample chamber dedicated to such systems.

It is divided into three main sections vertically arranged [Fig. 5(a)]. The bottom pumping section includes a turbopump and an ion pump in order to reach a pressure in the 10^{-9} mbar range. The middle measurement section includes the beamline port and the spectrometer with a scattering angle of 90°. The top section is dedicated to sample transfers from a load-lock and basic sample preparation capacity. The sample transfer system is compatible with a custom-built low-temperature suitcase for anaerobic transport of frozen solution from a glove box to the cooled sample holder in the UHV chamber, as well as with conventional UHV suitcases. A photograph of the spectrometer-sample chamber ensemble is shown in Fig. 5(b).

During preparations and measurements, samples are mounted on a custom multi-purpose sample holder system [Fig. 5(c)] attached to a vertical cryostat. The sample holder system consists of ten sample slots for conventional flag-style sample plates. The upper sample slot allows full temperature control of samples in the 10 to 300 K temperature range and is therefore dedicated mainly to studies on systems with peculiar temperature-dependent properties or with low-temperature phases of interest. The middle position with eight sample slots, two on each of the four sides of the sample holder, allows spectroscopy on samples held at 70 K or at room temperature. This part is especially designed for the measurements on many samples at intermediate low temperatures, like molecular systems in frozen solutions. The lowest position includes an additional electrical contact to allow, i.e., gate voltage-dependent measurements of quantum devices[36–39] at 70 K or at room temperature.

A custom helium closed-cycle cryostat is used in order to keep samples at a cooled and stable temperature during week(s)-long beamtimes without the need for liquid nitrogen or liquid helium. The cryostat is mounted on a fully motorized manipulator, which allows X, Y, Z, and θ fine sample positioning. The Z stroke enables translation from the upper transfer/preparation section to the middle measurement section.

B. Beamline

The performance of the spectrometer–sample chamber assembly is closely linked to the characteristics of the hosting beamline. The setup is installed as a permanent station at the UE52-SGM beamline branch with an elliptically polarizing undulator as the insertion device for full polarization control of the incident beam and with a photon flux of 10^{11}–10^{12} ph/s in the TES operational energy range 250–1000 eV.[40]

The setup shares the beamline branch with a second experimental station,[41] which is placed at the beamline focal point. The

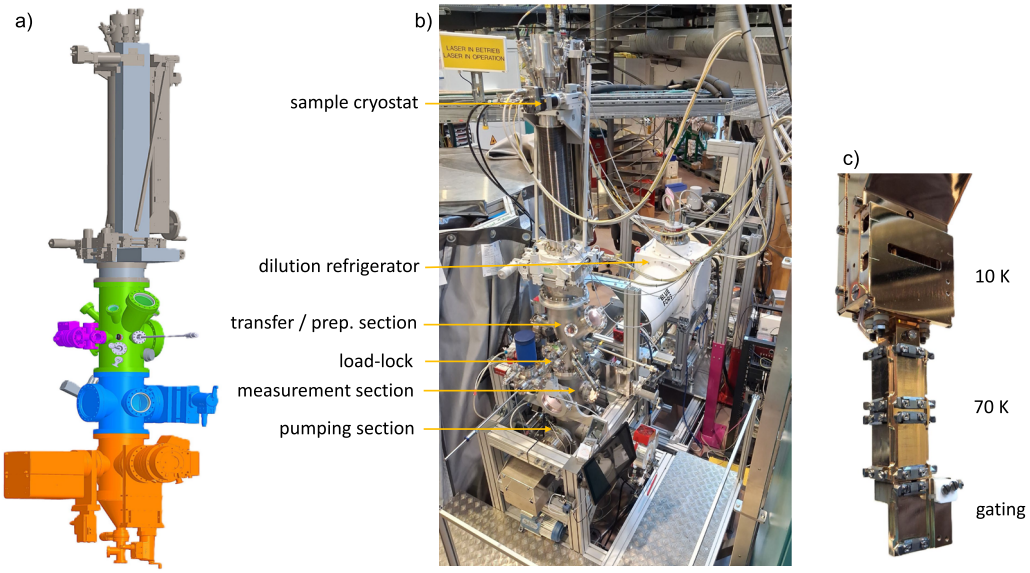

FIG. 5. Sample environment and full setup. (a) Sample chamber. Gray: sample cryostat and manipulator; green: sample transfer and sample preparation section; purple: suitcases-compatible fast-entry load-lock; blue: measurement section; and orange: pumping section. (b) Full setup photograph including the sample chamber and the spectrometer. (c) Low- and full temperature-controlled multi-sample holder, drawings, and photograph of the holder. Upper single sample position: T = 10–300 K with 0.1 K temperature control via a heater placed behind the sample. Middle eight-sample positions for T = 70 K or room temperature. Lower single sample position for T = 70 K or room temperature with an additional connection for applied voltage-dependent experiments.

TES is positioned 1 m away from the focus, resulting in a beam spot size of 6 mm (horizontal) × ~1 mm (vertical, depending on the beamline slit opening). The horizontal beam dimension can, however, be reduced if needed using inline baffles placed between the two end stations, for example, when having several small samples on a single sample plate.

IV. OPERATION, CHARACTERIZATION, AND PERFORMANCE

After describing the detector and experimental environment, we now characterize the spectrometer performance in terms of calibration procedure, energy resolution, count-rate capability, and long-term stability. The data from the TES array are processed using an optimal filter analysis method.[42,43] As a first step before actual measurements, the filter is constructed by measuring the detector noise (pulse-free data) and an "average" pulse shape for each sensor. The noise data are acquired by recording a few seconds of continuously triggered data with the beam shuttered. Then, to construct the average pulse shape model, the beam shutter is opened, and pulses are recorded for all sensors for about 1 min using the same edge trigger method that is used to acquire scientific data. The acquisition time for this step is about 1 min. Then, the noise and pulse shapes are used to compute an optimal filter for each sensor that is applied to all subsequent data. This procedure is typically conducted before each energy calibration.

The energy calibration is performed by recording an XES spectrum of a powder sample containing a mixture of graphite, boron nitride, Fe_2O_3, NiO, and CuO with an incident energy above the Cu L-edge (952.3 eV). The XES spectrum [Fig. 6(a)] presents the C Kα_1 at 277 eV, the N Kα_1 at 392.4 eV, the O Kα_1 at 524.9 eV, the Fe L$\alpha_{1,2}$ at 705 eV, the Ni L$\alpha_{1,2}$ at 851.5 eV, and the Cu L$\alpha_{1,2}$ at 929.7 eV emission peaks.[18,44] The optimally filtered pulse height vs energy is measured and fitted using a spline function for each sensor. Examples of calibrations for two sensors are presented in Fig. 6(b). Based on this calibration procedure, we evaluate the intrinsic energy resolution of the spectrometer across the accessible photon-energy range.

Figure 6(c) shows the signal corresponding to single photons of varying energies absorbed by a single sensor. The photon creates a pulse characterized by a fast increase of the detected signal, followed by a decay in the ms to a few ms range, depending on the sensor. Increasing the incoming photon energy results in an increase in the pulse height, accompanied by a slight change in the pulse shape.

The performance of the setup is illustrated by the energy resolution vs the energy of the incoming photons, the change in the measured photon rate and energy resolution as a function of the incoming photon flux, and the stability of features over time.

The energy resolution vs incoming photon energy is estimated by measuring the FWHM of the elastic scattering feature from a gold thin film on a silicon substrate with vertical polarization for a set of energies ranging from 260 to 890 eV. The results are described in Fig. 7(a). Each detected photon is characterized by its energy, and the detection time is characterized by the array and the detecting channel. Sensors can slightly differ in their intrinsic detection rate and intrinsic energy resolution as well as in the accuracy of the measured energy with respect to the nominal incoming photon energy. The latter depends on the quality of the calibration and

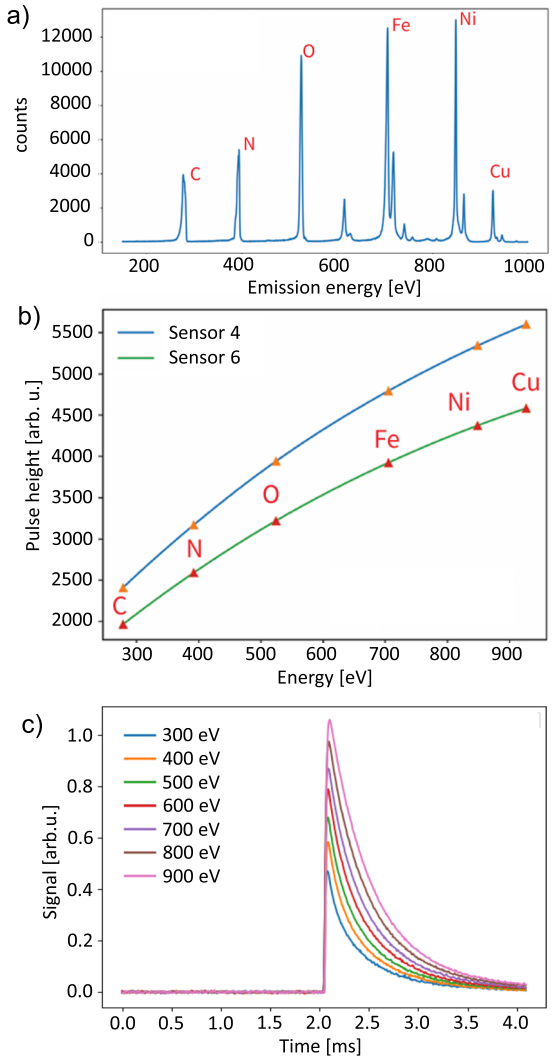

FIG. 6. Energy calibration. (a) XES spectrum acquired on the powder mixture for emission peak assignment. $h\nu$ = 980 eV, linear horizontal incoming beam polarization. Acquisition time is 30 min. (b) Example of energy vs pulse height spline fit for two sensors. (c) Pulse profile of one sensor's response to a series of incident photons with energies of 300–900 eV.

can be improved by, e.g., increasing the proximity of the features of interest to the calibration lines by having more elements and, therefore, more emission lines in the calibration mixture. Accordingly, Fig. 7(a) summarizes the results obtained using three different evaluation methods to estimate the resolution: the co-added sum, the unweighted, and the weighted FWHM. For the co-added sum approach, the FWHM is fitted from all sensors, including their individual slight deviation from the perfect case in energy calibration, which broadens the sum of elastic scattering features and their different intensities. For the weighted method, the FWHM is fitted for all sensors independently, disregarding the energy shift from the calibration error but weighted by their respective detected photon counts before summing. For the unweighted method, the FWHM

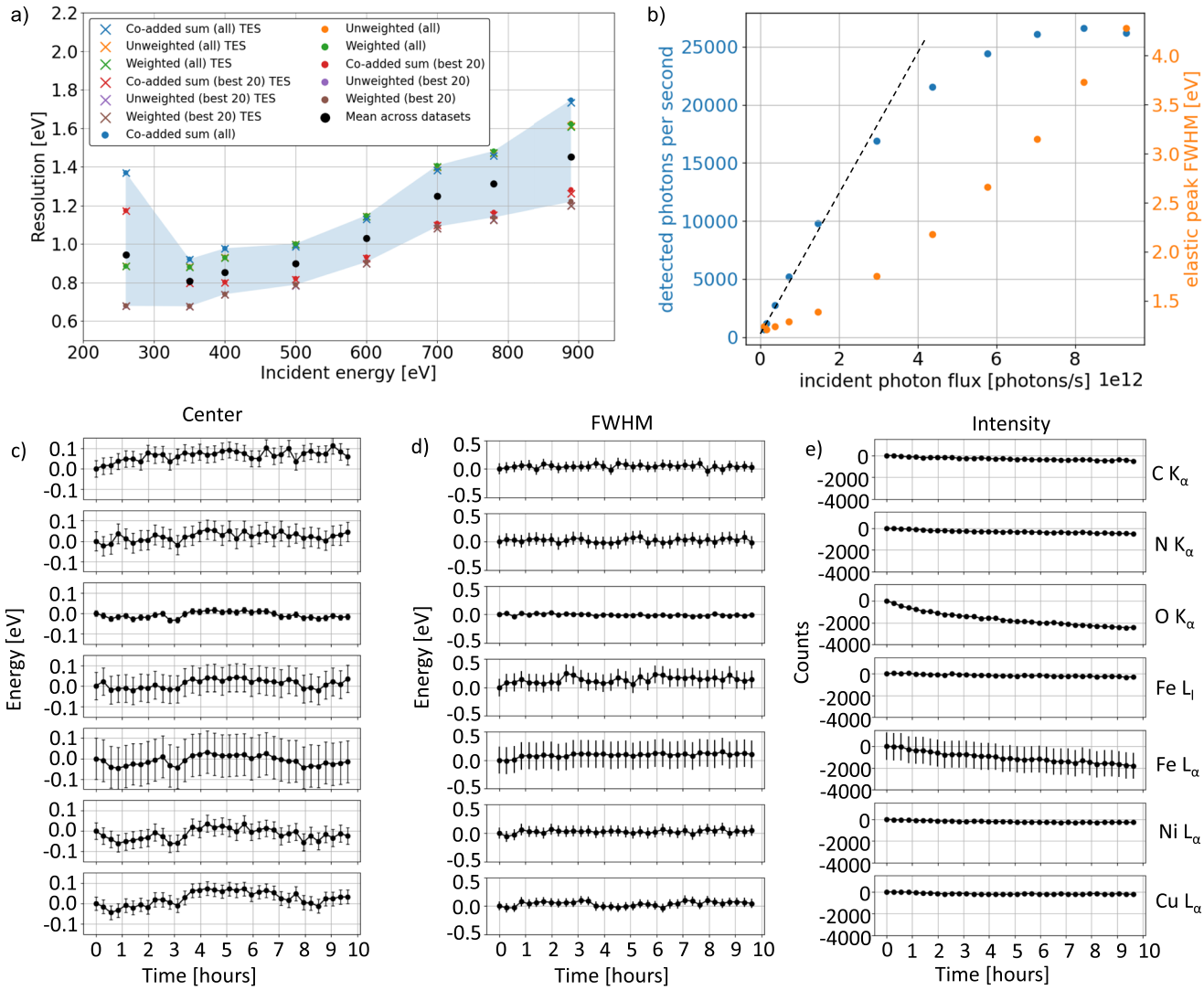

FIG. 7. Instrument performance. (a) Energy resolution vs incoming photon energy. Dots are the total resolution; crosses are the intrinsic spectrometer resolution with the quadratic component of the beamline resolution subtracted. Blue, orange, and green are the co-added, unweighted, and weighted (see text) energy resolutions of the full array. Red, purple, and brown are the co-added, unweighted, and weighted energy resolutions of the 20 best-resolution sensors. (b) Count rate saturation characteristics. Blue: Detected counts per second vs incoming flux. The dotted line is a guide to the eye and represents the idealized saturation-free limit, valid at low photon flux. Orange: Co-added elastic peak FWHM vs incoming flux. [(c)–(e)] Evolution of the energy center, FWHM, and intensity, respectively, of the C, N, O, Fe, Ni, and Cu emission peaks in Fig. 6(a) vs time over 10 h. The error bars are the uncertainty of the Gaussian fits.

is also fitted for all sensors independently but with an equal contribution for all sensors before summing, normalizing the detected photon count differences. In Fig. 7(a), we show the results for the full array and for the twenty sensors with the best resolution (colored circle dots). The corresponding resolutions, subtracting the contribution of the beamline energy resolution, are also shown (colored crosses).[18] The black dots are the average over all methods, and the gray area defines the uncertainty.

We measure a resolution of 0.7–1.7 eV in the region 260–890 eV, with an almost linear increase with the energy. The twenty best channels present a ~10%–20% better resolution than the full array, with the best intrinsic resolution below 0.8 eV averaged over the twenty best sensors, for incident energies below 500 eV. Interestingly, we observe that the difference between the co-added (blue) and the unweighted (orange) points differs more at the energy range extrema. In addition, we observe a coarsened resolution below 300 eV, which we attribute to the broad C emission peak in the calibration [see Fig. 6(a)]. This highlights the importance of the calibration process to successfully combine the spectra from different sensors. These measurements were

performed before fine optimizations for mechanical and electrical noise reduction.

In addition to spectral resolution, the maximum useable photon rate is another key performance parameter of TES spectrometers. Pulse pile-up effect at high photon flux can occur due to the ms to few ms fall time back to the operating temperature after an incoming photon [Figs. 2(c) and 6(c)]. To characterize the pile-up response of the spectrometer, we measured the detected count rate and FWHM of the elastic line when illuminating a bulk copper target with an incoming photon energy $h\nu = 550$ eV, tuning the photon flux via the beamline exit slit.

Figure 7(b) shows that the detected counts linearly increase, followed by a deviation of the count rate when increasing the incoming photon flux. The low photon flux side corresponds to the case of the absence of pile-up, where each photon from the target is counted when hitting a sensor and, therefore, defines the ideal detection rate of the array, as shown by the dotted line. At about 10 000 detected counts per second, the pile-up starts. This count rate limitation defines the dominant constraint on acquisition efficiency in high-flux conditions rather than detector transmission losses. The readout software has three modes for photon detection (triggering), which change how pile-up events are handled. In one case, if a second triggering occurs within one pulse record, two shorter length records are written. A second mode consists of discarding the record when two triggers are detected, i.e., to write nothing to disk. A third mode is to write one regular-length record that contains both events, which can later be cut in analysis.[45] We are operating in the second detection mode. Therefore, the increasing deviation from the ideal rate corresponds to the increasing number of rejected events. The FWHM of the elastic peak increases with the photon flux. This increase occurs before the deviation from the ideal case of the detection rate. Therefore, during experiments, a balance between a reasonable detection count rate and energy resolution must be found. In practice, during experiments for which a high resolution is crucial, a detected count rate of 2000–5000 counts per second is set by tuning the beamline openings. It must be noted that the tuning of the incident photon flux was performed by tuning the beamline horizontal opening slit. Therefore, the vertical beam size at the sample position is larger for higher flux (from a few tenths of mm for the lowest flux to 4 mm for the highest). In addition, the bulk copper target has an extremely high fluorescence yield compared to the low-dimensional and low-concentration systems for which the setup has been designed.

Another important parameter for practical synchrotron operation is the long-term stability of the detector response. Earlier generations of TES detectors at synchrotron facilities included adiabatic demagnetization refrigerators (ADR), which have limited stability of spectral features over time due to temperature variations and necessitate regular recalibration and drift corrections.[18] The stability is defined as the deviation in energy, FWHM, and amplitude with time of a given spectral feature. Instead of an ADR, the present setup uses a DR to keep the detector at its operating temperature. To characterize the stability, we performed repeated XES spectra of the calibration mixture (Fig. 6) right after a calibration. Figures 7(c)–7(e) show the evolution of the energies, FWHM, and amplitudes over time of the seven emission features depicted in Fig. 6. Each data point time corresponds to the beginning of a XES acquisition. We observe an energy stability better than 0.1 eV over almost 10 h, without the monotonic drift observed with ADR-based TES. Similarly, we observe no loss of energy resolution over time. We note a decrease in the amplitude of emission features, which we attribute to beam damage to the mixture over such an extended exposure time. Therefore, in practice, only one calibration at the beginning of a beamtime shift is *a priori* necessary. Having established the spectrometer performance, we now illustrate its capabilities through representative measurements on low-dimensional and dilute systems.

V. EXAMPLES OF XES MEASUREMENTS

A. Monolayer h-BN

Hexagonal boron nitride (h-BN) is an insulating van der Waals (layered) material with a crossover from an indirect bandgap of 5.95 eV in bulk to a direct bandgap of 6.1 eV in the monolayer case.[46] Within single layers, boron and nitrogen atoms are sp^2 bonded to form a 2D hexagonal lattice (honeycomb structure) comparable to graphene. XES at the boron and nitrogen K-edges was used to detect exciton and plasmon excitations in the scattering process at

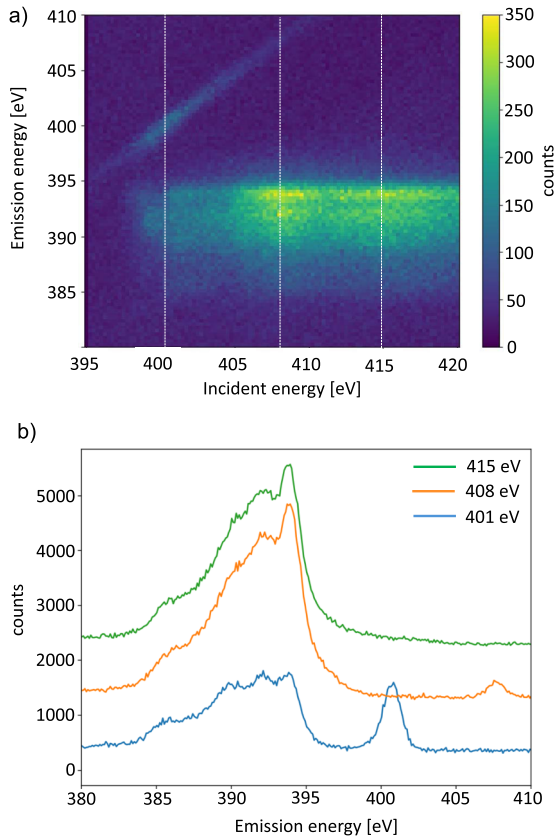

FIG. 8. Test experiment on the monolayer h-BN system. (a) RIXS-map at the N K-edge (3-h acquisition). (b) Single emission spectra acquired at $h\nu = 401$, 408, and 415 eV [see the white lines in (a)]. Spectra are shifted vertically for clarity (1-h acquisition for each spectrum).

resonance and to probe the influence of the materials around single layers.[47–50] Here, to demonstrate the capabilities of the setup to perform XES on atomically thin materials with acquisition times compatible with synchrotron beamtime operation, we performed measurements at the nitrogen K-edge on a monolayer of h-BN on SiO_2, capped by graphene.[51,52]

The results are presented in Fig. 8. The RIXS-map in Fig. 8(a) presents two main features: the elastic scattering line ($E_{em.} = E_{inc.}$) and constant emission-energy lines in the range $E_{em.}$ = 385–395 eV, at and above threshold at $E_{inc.} \sim 400$ eV. Single XES spectra at $E_{inc.}$ = 401, 408, and 415 eV are shown in Fig. 8(b). Spectra acquired for $E_{inc.} > 415$ eV show no significant change in shape due to strong phonon–exciton coupling in h-BN.[50] Close to resonance, XES presents features at 394, 392, 390, and 396 eV. The energy of these features does not depend on the incident energy and has thus been interpreted as fluorescence lines attributed to the radiative decay from the valence band, explaining the line shape related to the valence p-DOS.[49,50,53]

The RIXS-map in Fig. 8(a) and XES single spectra in Fig. 8(b) were acquired in 3 and 1 h, respectively, which demonstrates the capacity of the setup to perform measurements at the atomic monolayer limit in a reasonable time and, due to the relatively low photon flux needed, without beam damage.

B. Sub-millimolar $K_3[Fe(CN)_6]$ in frozen water solution

While the previous example demonstrates measurements at the atomic monolayer limit in a solid-state system, the following example illustrates performance in the extreme case of sub-millimolar molecular concentrations. As a second example, we present in Fig. 9 the extreme case of Fe L-edge XAS and RIXS measurements of a 0.5 mM concentration ferricyanide $K_3[Fe(CN)_6]$ solution system.[18,44] The pure compound was diluted in water and frozen with liquid nitrogen before transfer to the sample chamber using a custom UHV vacuum low-temperature suitcase, which allows the transport and pumping of frozen solutions at liquid nitrogen temperature. After attaching the suitcase to the load-lock and pumping, the sample plate is transferred to the sample holder in the main chamber. These experiments were performed at a temperature of 70 K. A series of spectra was acquired during 10 h and summed. No loss of frozen solution was observed. The comparison of spectra in the acquisition series shows low beam damage.

The partial fluorescence yield (PFY) XAS spectra shown in Fig. 9(b) are derived from the RIXS map in Fig. 9(a) by integrating emission energy regions vs the incident energy. The Lα + Lβ as well as the Lα PFY-XAS are characterized by the two split L_3 and L_2 main features at $E_{incident}$ = 710 and 723 eV, respectively. The characteristic 706–710 eV splitting due to the presence of a hole in the t_{2g} manifold is clearly visible in the RIXS map, the Lα + Lβ as well as the Lα PFY-XAS. The feature at 705.8 eV and at the vicinity of 710 eV correspond to 2p → 3d transitions while the feature at 712.3 eV corresponds to a 2p → CN(π^*) transition.[54] Both absorption and emission spectra present a reasonable signal to noise ratio.[18,44] This example demonstrates the capability of the setup to perform RIXS experiments on sub-millimolar molecular systems, a concentration regime not accessible using WD spectrometers in a reasonable acquisition time. These example measurements highlight the versatility of the instrument across a broad range of sample classes and concentration regimes.

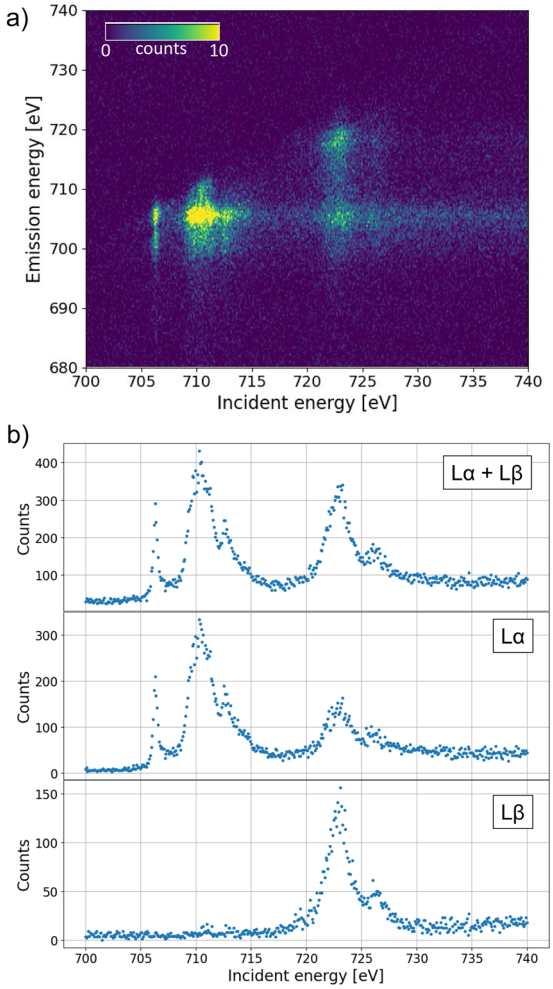

FIG. 9. Test the experiment on the frozen 0.5 mM concentration of $K_3[Fe(CN)_6]$ in water. (a) RIXS map at the Lα and Lβ energy regions. (b) PFY XAS derived from the RIXS map. The Lα + Lβ spectrum includes the emission region 680–740 eV. The Lα spectrum includes the emission region 700–712 eV. The Lβ spectrum includes the emission region 712–724 eV. The acquisition time is 10 h with horizontally polarized light.

VI. CONCLUSION

The next-generation of TES array XES spectrometer commissioned at BESSY II, based on microwave SQUID multiplexing readout and DR cryogenics, demonstrates unprecedented performance in terms of collecting efficiency, energy resolution, saturation, and stability. The presented instrument enables XAS, XES, and RIXS investigations of low-dimensional and low-concentration systems, so far unexplored with soft x-ray XES and RIXS techniques, including atomically thin materials, impurity-level quantum systems, nanostructures, gated devices, and dilute molecular and protein systems. The sample environment of the setup allows the transfer and

preparation of such systems with precise temperature control from 10 K to room temperature. Further developments of the setup in terms of sample preparation and magnetic circular dichroism in emission (RIXS-MCD),[55,56] for which additional magnetic shielding around the detector is already present, are envisaged.

Fundamentally, the development of TES arrays for synchrotron applications represents a new paradigm for XES and RIXS instrumentation, not competing with WD spectrometers in terms of resolution power but complementary to them. Following this aspect, the use of TESs for XES, which probes the filled valence bands in solids and the density of low-lying excited states in atomic and molecular systems,[57] even allows so-called RIXS band-mapping.[58] Therefore, XES performed with TESs becomes complementary to angle-resolved photoemission spectroscopy (ARPES), offering element- and orbital-selective access to occupied electronic states, even on insulating samples. Finally, it opens the route to XES and RIXS experiments on physical systems so far only accessible to ARPES.

ACKNOWLEDGMENTS

We acknowledge the BESSY staff for their technical support and Sang-Jun Lee for fruitful discussions.

AUTHOR DECLARATIONS

Conflict of Interest

The authors have no conflicts to disclose.

Author Contributions

Régis Decker: Conceptualization (equal); Formal analysis (equal); Investigation (equal); Methodology (equal); Writing – original draft (lead). **Kelsey M. Morgan**: Conceptualization (equal); Formal analysis (equal); Investigation (equal); Methodology (equal); Writing – review & editing (equal). **Sergey Peredkov**: Formal analysis (equal); Investigation (equal); Methodology (equal); Writing – review & editing (equal). **Charles J. Titus**: Formal analysis (equal); Methodology (equal); Software (equal); Writing – review & editing (equal). **Galen C. O'Neil**: Formal analysis (equal); Methodology (equal); Software (equal); Writing – review & editing (equal). **Alexander Dillmann**: Formal analysis (equal); Methodology (equal); Software (equal); Writing – review & editing (equal). **Dmitry Tikhonov**: Formal analysis (equal); Methodology (equal); Software (equal); Writing – review & editing (equal). **Utkarsh Prakash**: Investigation (equal); Methodology (equal); Writing – review & editing (equal). **Axel Knop-Gericke**: Investigation (equal); Methodology (equal); Writing – review & editing (equal). **Joseph W. Fowler**: Formal analysis (equal); Methodology (equal); Software (equal); Writing – review & editing (equal). **Jonathan W. Dean**: Formal analysis (equal); Methodology (equal); Software (equal); Writing – review & editing (equal). **Nathan Nakamura**: Formal analysis (equal); Methodology (equal); Software (equal); Writing – review & editing (equal). **Raoul Blume**: Investigation (equal); Methodology (equal); Writing – review & editing (equal). **Detre Techner**: Investigation (equal); Methodology (equal); Writing – review & editing (equal). **Minmin Chen**: Investigation (equal); Methodology (equal); Writing – review & editing (equal). **Zechao Jin**: Methodology (equal); Resources (equal); Writing – review & editing (equal). **Christian Weniger**: Methodology (equal); Resources (equal); Writing – review & editing (equal). **Thomas Blume**: Methodology (equal); Resources (equal); Writing – review & editing (equal). **Torsten Kachel**: Conceptualization (equal); Methodology (equal); Resources (equal); Writing – review & editing (equal). **Nathan J. Ortiz**: Methodology (equal); Resources (equal); Writing – review & editing (equal). **Douglas A. Bennett**: Methodology (equal); Resources (equal); Writing – review & editing (equal). **John A. B. Mates**: Methodology (equal); Resources (equal); Writing – review & editing (equal). **Daniel R. Schmidt**: Methodology (equal); Resources (equal); Writing – review & editing (equal). **Jozsef Imrek**: Methodology (equal); Resources (equal); Writing – review & editing (equal). **Joel C. Weber**: Methodology (equal); Resources (equal); Writing – review & editing (equal). **Johnathon D. Gard**: Methodology (equal); Resources (equal); Software (equal); Writing – review & editing (equal). **Leila Vale**: Methodology (equal); Resources (equal); Writing – review & editing (equal). **Abigail L. Wessels**: Methodology (equal); Resources (equal); Writing – review & editing (equal). **Bastian Klemke**: Investigation (equal); Resources (equal); Writing – review & editing (equal). **Sebastian Gerischer**: Resources (equal); Writing – review & editing (equal). **Mattis Fondell**: Investigation (equal); Resources (equal); Writing – review & editing (equal). **Sebastian Eckert**: Investigation (equal); Resources (equal); Writing – review & editing (equal). **Joel N. Ullom**: Methodology (equal); Resources (equal); Writing – review & editing (equal). **Daniel S. Swetz**: Conceptualization (equal); Funding acquisition (equal); Supervision (equal); Writing – review & editing (equal). **Serena DeBeer**: Conceptualization (equal); Funding acquisition (equal); Supervision (equal); Writing – review & editing (equal). **Alexander Föhlisch**: Conceptualization (equal); Funding acquisition (equal); Supervision (equal); Writing – review & editing (equal).

DATA AVAILABILITY

The data that support the findings of this study are available from the corresponding author upon reasonable request.

REFERENCES

[1] J. Stöhr, *NEXAFS Spectroscopy* (Springer-Verlag, 1996), Vol. 6, p. 8262.
[2] F. de Groot and A. Kotani, *Core Level Spectroscopy of Solids* (CRC Press, 2008), Vol. 6, p. 8262.
[3] L. J. P. Ament, M. van Veenendaal, T. P. Devereaux, J. P. Hill, and J. van den Brink, "Resonant inelastic x-ray scattering studies of elementary excitations," Rev. Mod. Phys. **83**, 705–767 (2011).
[4] G. E. Cutsail III and S. DeBeer, "Challenges and opportunities for applications of advanced x-ray spectroscopy in catalysis research," ACS Catal. **12**, 5864–5886 (2022).
[5] M. Beye, F. Hennies, M. Deppe, E. Suljoti, M. Nagasono, W. Wurth, and A. Föhlisch, "Dynamics of electron-phonon scattering: Crystal-and angular-momentum transfer probed by resonant inelastic x-ray scattering," Phys. Rev. Lett. **103**, 237401 (2009).
[6] R. Decker, A. Born, R. Büchner, K. Ruotsalainen, C. Stråhlman, S. Neppl, R. Haverkamp, A. Pietzsch, and A. Föhlisch, "Measuring the atomic spin-flip scattering rate by x-ray emission spectroscopy," Sci. Rep. **9**, 8977 (2019).
[7] A. Born, R. Decker, R. Büchner, R. Haverkamp, K. Ruotsalainen, K. Bauer, A. Pietzsch, and A. Föhlisch, "Thresholding of the Elliott–Yafet spin-flip scattering in

multi-sublattice magnets by the respective exchange energies," Sci. Rep. **11**, 1883 (2021).
[8]R. Decker, A. Born, K. Ruotsalainen, K. Bauer, R. Haverkamp, R. Büchner, A. Pietzsch, and A. Föhlisch, "Spin-lattice angular momentum transfer of localized and valence electrons in the demagnetization transient state of gadolinium," Appl. Phys. Lett. **119**, 152403 (2021).
[9]V. N. Strocov, T. Schmitt, U. Flechsig, T. Schmidt, A. Imhof, Q. Chen, J. Raabe, R. Betemps, D. Zimoch, J. Krempasky, X. Wang, M. Grioni, A. Piazzalunga, and L. Patthey, "High-resolution soft X-ray beamline ADDRESS at the Swiss light source for resonant inelastic X-ray scattering and angle-resolved photoelectron spectroscopies," J. Synchrotron Radiat. **17**, 631–643 (2010).
[10]N. B. Brookes, F. Yakhou-Harris, K. Kummer, A. Fondacaro, J. C. Cezar, D. Betto, E. Velez-Fort, A. Amorese, G. Ghiringhelli, L. Braicovich, R. Barrett, G. Berruyer, F. Cianciosi, L. Eybert, P. Marion, P. van der Linden, and L. Zhang, "The beamline ID32 at the ESRF for soft x-ray high energy resolution resonant inelastic x-ray scattering and polarisation dependent x-ray absorption spectroscopy," Nucl. Instrum. Methods Phys. Res., Sect. A **903**, 175–192 (2018).
[11]J. Schlappa, G. Ghiringhelli, B. E. Van Kuiken, M. Teichmann, P. S. Miedema, J. T. Delitz, N. Gerasimova, S. Molodtsov, L. Adriano, B. Baranasic, C. Broers, R. Carley, P. Gessler, N. Ghodrati, D. Hickin, L. P. Hoang, M. Izquierdo, L. Mercadier, G. Mercurio, S. Parchenko, M. Stupar, Z. Yin, L. Martinelli, G. Merzoni, Y. Y. Peng, T. Reuss, S. Sreekantan Nair Lalithambika, S. Techert, T. Laarmann, S. Huotari, C. Schroeter, B. Langer, T. Giessel, J. Buchheim, G. Gwalt, A. Sokolov, F. Siewert, R. Buechner, V. Vaz da Cruz, S. Eckert, C.-Y. Liu, C. Sohrt, C. Weniger, A. Pietzsch, S. Neppl, F. Senf, A. Scherz, and A. Föhlisch, "The Heisenberg-RIXS instrument at the European XFEL," J. Synchrotron Radiat. **32**, 29–45 (2025).
[12]M. Agåker, C.-J. Englund, V. Ekholm, L. Kjellsson, P. Sjöblom, L. Pickworth, J. Söderström, N. Johansson, A. Ghosh, T. Tokushima, M. Caputo, J. Forsberg, G. Felcsuti, P. Fredriksson, S. Malki, N. Wassdahl, C. Såthe, and J.-E. Rubensson, "The 10 m collimated Rowland spectrometer at the MAX IV Veritas beamline," J. Synchrotron Radiat. **32**, 1328–1345 (2025).
[13]I. Jarrige, V. Bisogni, Y. Zhu, W. Leonhardt, and J. Dvorak, "Paving the way to ultra-high-resolution resonant inelastic x-ray scattering with the six beamline at NSLS-II," Synchrotron Radiat. News **31**, 7–13 (2018).
[14]W. B. Doriese, P. Abbamonte, B. K. Alpert, D. A. Bennett, E. V. Denison, Y. Fang, D. A. Fischer, C. P. Fitzgerald, J. W. Fowler, J. D. Gard, J. P. Hays-Wehle, G. C. Hilton, C. Jaye, J. L. McChesney, L. Miaja-Avila, K. M. Morgan, Y. I. Joe, G. C. O'Neil, C. D. Reintsema, F. Rodolakis, D. R. Schmidt, H. Tatsuno, J. Uhlig, L. R. Vale, J. N. Ullom, and D. S. Swetz, "A practical superconducting-microcalorimeter x-ray spectrometer for beamline and laboratory science," Rev. Sci. Instrum. **88**, 053108 (2017).
[15]J. Uhlig, W. B. Doriese, J. W. Fowler, D. S. Swetz, C. Jaye, D. A. Fischer, C. D. Reintsema, D. A. Bennett, L. R. Vale, U. Mandal, G. C. O'Neil, L. Miaja-Avila, Y. I. Joe, A. El Nahhas, W. Fullagar, F. Parnefjord Gustafsson, V. Sundström, D. Kurunthu, G. C. Hilton, D. R. Schmidt, and J. N. Ullom, "High-resolution x-ray emission spectroscopy with transition-edge sensors: Present performance and future potential," J. Synchrotron Radiat. **22**, 766–775 (2015).
[16]Y. I. Joe, Y. Fang, S. Lee, S. X. L. Sun, G. A. de la Peña, W. B. Doriese, K. M. Morgan, J. W. Fowler, L. R. Vale, F. Rodolakis, J. L. McChesney, J. N. Ullom, D. S. Swetz, and P. Abbamonte, "Resonant soft x-ray scattering from stripe-ordered $La_{2-x}Ba_xCuO_4$ detected by a transition-edge sensor array detector," Phys. Rev. Appl. **13**, 034026 (2020).
[17]J. N. Ullom and D. A. Bennett, "Review of superconducting transition-edge sensors for x-ray and gamma-ray spectroscopy," Supercond. Sci. Technol. **28**, 084003 (2015).
[18]S.-J. Lee, C. J. Titus, R. Alonso Mori, M. L. Baker, D. A. Bennett, H.-M. Cho, W. B. Doriese, J. W. Fowler, K. J. Gaffney, A. Gallo, J. D. Gard, G. C. Hilton, H. Jang, Y. I. Joe, C. J. Kenney, J. Knight, T. Kroll, J.-S. Lee, D. Li, D. Lu, R. Marks, M. P. Minitti, K. M. Morgan, H. Ogasawara, G. C. O'Neil, C. D. Reintsema, D. R. Schmidt, D. Sokaras, J. N. Ullom, T.-C. Weng, C. Williams, B. A. Young, D. S. Swetz, K. D. Irwin, and D. Nordlund, "Soft x-ray spectroscopy with transition-edge sensors at Stanford synchrotron radiation lightsource beamline 10-1," Rev. Sci. Instrum. **90**, 113101 (2019).
[19]U. Patel, T. Guruswamy, A. J. Krzysko, H. Charalambous, L. Gades, K. Wiaderek, O. Quaranta, Y. Ren, A. Yakovenko, U. Ruett, and A. Miceli, "High-resolution Compton spectroscopy using x-ray microcalorimeters," Rev. Sci. Instrum. **93**, 113105 (2022).
[20]S. Yamada, Y. Ichinohe, H. Tatsuno, R. Hayakawa, H. Suda, T. Ohashi, Y. Ishisaki, T. Uruga, O. Sekizawa, K. Nitta, Y. Takahashi, T. Itai, H. Suga, M. Nagasawa, M. Tanaka, M. Kurisu, T. Hashimoto, D. Bennett, E. Denison, W. B. Doriese, M. Durkin, J. Fowler, G. O'Neil, K. Morgan, D. Schmidt, D. Swetz, J. Ullom, L. Vale, S. Okada, T. Okumura, T. Azuma, T. Tamagawa, T. Isobe, S. Kohjiro, H. Noda, K. Tanaka, A. Taguchi, Y. Imai, K. Sato, T. Hayashi, T. Kashiwabara, and K. Sakata, "Broadband high-energy resolution hard x-ray spectroscopy using transition edge sensors at spring-8," Rev. Sci. Instrum. **92**, 013103 (2021).
[21]H. Kraus, "Superconductive bolometers and calorimeters," Supercond. Sci. Technol. **9**, 827 (1996).
[22]S. P. Langley, *Annals of the Astrophysical Observatory of the Smithsonian Institution* (Smithsonian Institution, Washington, DC, 1900), Vol. 1.
[23]S. P. T., "The bolometer," Nature **25**, 14–16 (1881).
[24]D. H. Andrews, R. D. Fowler, and M. C. Williams, "The effect of alpha-particles on a superconductor," Phys. Rev. **76**, 154–155 (1949).
[25]K. D. Irwin, "An application of electrothermal feedback for high resolution cryogenic particle detection," Appl. Phys. Lett. **66**, 1998–2000 (1995).
[26]J. C. Weber, K. M. Morgan, D. Yan, C. G. Pappas, A. L. Wessels, G. C. O'Neil, D. A. Bennett, G. C. Hilton, D. S. Swetz, J. N. Ullom, and D. R. Schmidt, "Development of a transition-edge sensor bilayer process providing new modalities for critical temperature control," Supercond. Sci. Technol. **33**, 115002 (2020).
[27]J. A. Chervenak, K. D. Irwin, E. N. Grossman, J. M. Martinis, C. D. Reintsema, and M. E. Huber, "Superconducting multiplexer for arrays of transition edge sensors," Appl. Phys. Lett. **74**, 4043–4045 (1999).
[28]J. Yoon, J. Clarke, J. M. Gildemeister, A. T. Lee, M. J. Myers, P. L. Richards, and J. T. Skidmore, "Single superconducting quantum interference device multiplexer for arrays of low-temperature sensors," Appl. Phys. Lett. **78**, 371–373 (2001).
[29]D. T. Becker, D. A. Bennett, M. Biasotti, M. Borghesi, V. Ceriale, M. D. Gerone, M. Faverzani, E. Ferri, J. W. Fowler, G. Gallucci, J. D. Gard, A. Giachero, J. P. Hays-Wehle, G. C. Hilton, J. A. B. Mates, A. Nucciotti, A. Orlando, G. Pessina, A. Puiu, C. D. Reintsema, D. R. Schmidt, D. S. Swetz, J. N. Ullom, and L. R. Vale, "Working principle and demonstrator of microwave-multiplexing for the Holmes experiment microcalorimeters," J. Instrum. **14**, P10035 (2019).
[30]J. A. B. Mates, D. T. Becker, D. A. Bennett, B. J. Dober, J. D. Gard, J. P. Hays-Wehle, J. W. Fowler, G. C. Hilton, C. D. Reintsema, D. R. Schmidt, D. S. Swetz, L. R. Vale, and J. N. Ullom, "Simultaneous readout of 128 x-ray and gamma-ray transition-edge microcalorimeters using microwave squid multiplexing," Appl. Phys. Lett. **111**, 062601 (2017).
[31]J. A. B. Mates, D. T. Becker, D. A. Bennett, B. J. Dober, J. D. Gard, G. C. Hilton, D. S. Swetz, L. R. Vale, and J. N. Ullom, "Crosstalk in microwave squid multiplexers," Appl. Phys. Lett. **115**, 202601 (2019).
[32]J. A. B. Mates, K. D. Irwin, L. R. Vale, G. C. Hilton, J. Gao, and K. W. Lehnert, "Flux-ramp modulation for squid multiplexing," J. Low Temp. Phys. **167**, 707–712 (2012).
[33]J. Nordgren, G. Bray, S. Cramm, R. Nyholm, J.-E. Rubensson, and N. Wassdahl, "Soft x-ray emission spectroscopy using monochromatized synchrotron radiation (invited)," Rev. Sci. Instrum. **60**, 1690–1696 (1989).
[34]K. Bauer, J.-S. Schmidt, F. Eggenstein, R. Decker, K. Ruotsalainen, A. Pietzsch, T. Blume, C.-Y. Liu, C. Weniger, F. Siewert, J. Buchheim, G. Gwalt, F. Senf, P. Bischoff, L. Schwarz, K. Effland, M. Mast, T. Zeschke, I. Rudolph, A. Meißner, and A. Föhlisch, "The meV XUV-RIXS facility at UE112-PGM1 of BESSY II," J. Synchrotron Radiat. **29**, 908–915 (2022).
[35]C. Schulz, K. Lieutenant, J. Xiao, T. Hofmann, D. Wong, and K. Habicht, "Characterization of the soft X-ray spectrometer PEAXIS at BESSY II," J. Synchrotron Radiat. **27**, 238–249 (2020).
[36]K. S. Novoselov, A. K. Geim, S. V. Morozov, D. Jiang, Y. Zhang, S. V. Dubonos, I. V. Grigorieva, and A. A. Firsov, "Electric field effect in atomically thin carbon films," Science **306**, 666–669 (2004).
[37]Y. Deng, Y. Yu, Y. Song, J. Zhang, N. Z. Wang, Z. Sun, Y. Yi, Y. Z. Wu, S. Wu, J. Zhu, J. Wang, X. H. Chen, and Y. Zhang, "Gate-tunable room-temperature ferromagnetism in two-dimensional Fe_3GeTe_2," Nature **563**, 94–99 (2018).
[38]V. W. Brar, S. Wickenburg, M. Panlasigui, C.-H. Park, T. O. Wehling, Y. Zhang, R. Decker, Ç. Girit, A. V. Balatsky, S. G. Louie, A. Zettl, and M. F. Crommie, "Observation of carrier-density-dependent many-body effects in graphene via tunneling spectroscopy," Phys. Rev. Lett. **104**, 036805 (2010).

[39]V. W. Brar, R. Decker, H.-M. Solowan, Y. Wang, L. Maserati, K. T. Chan, H. Lee, Ç. O. Girit, A. Zettl, S. G. Louie, M. L. Cohen, and M. F. Crommie, "Gate-controlled ionization and screening of cobalt adatoms on a graphene surface," Nat. Phys. **7**, 43–47 (2011).
[40]P. S. Miedema, W. Quevedo, and M. Fondell, "The variable polarization undulator beamline UE52 SGM at BESSY II," J. Large-Scale Res. Facilities **2**, A70 (2016).
[41]M. Fondell, S. Eckert, R. M. Jay, C. Weniger, W. Quevedo, J. Niskanen, B. Kennedy, F. Sorgenfrei, D. Schick, E. Giangrisostomi, R. Ovsyannikov, K. Adamczyk, N. Huse, P. Wernet, R. Mitzner, and A. Föhlisch, "Time-resolved soft x-ray absorption spectroscopy in transmission mode on liquids at MHz repetition rates," Struct. Dyn. **4**, 054902 (2017).
[42]A. E. Szymkowiak, R. L. Kelley, S. H. Moseley, and C. K. Stahle, "Signal processing for microcalorimeters," J. Low Temp. Phys. **93**, 281–285 (1993).
[43]E. Figueroa-Feliciano, B. Cabrera, A. J. Miller, S. F. Powell, T. Saab, and A. B. C. Walker, "Optimal filter analysis of energy-dependent pulse shapes and its application to TES detectors," Nucl. Instrum. Methods Phys. Res., Sect. A **444**, 453–456 (2000).
[44]C. J. Titus, M. L. Baker, S. J. Lee, H.-M. Cho, W. B. Doriese, J. W. Fowler, K. Gaffney, J. D. Gard, G. C. Hilton, C. Kenney, J. Knight, D. Li, R. Marks, M. P. Minitti, K. M. Morgan, G. C. O'Neil, C. D. Reintsema, D. R. Schmidt, D. Sokaras, D. S. Swetz, J. N. Ullom, T.-C. Weng, C. Williams, B. A. Young, K. D. Irwin, E. I. Solomon, and D. Nordlund, "L-edge spectroscopy of dilute, radiation-sensitive systems using a transition-edge-sensor array," J. Chem. Phys. **147**, 214201 (2017).
[45]J. W. Fowler, B. K. Alpert, W. B. Doriese, D. A. Fischer, C. Jaye, Y. I. Joe, G. C. O'Neil, D. S. Swetz, and J. N. Ullom, "Microcalorimeter spectroscopy at high pulse rates: A multi-pulse fitting technique," Astrophys. J. Suppl. Ser. **219**, 35 (2015).
[46]C. Elias, P. Valvin, T. Pelini, A. Summerfield, C. J. Mellor, T. S. Cheng, L. Eaves, C. T. Foxon, P. H. Beton, S. V. Novikov, B. Gil, and G. Cassabois, "Direct band-gap crossover in epitaxial monolayer boron nitride," Nat. Commun. **10**, 2639 (2019).
[47]J. J. Jia, T. A. Callcott, E. L. Shirley, J. A. Carlisle, L. J. Terminello, A. Asfaw, D. L. Ederer, F. J. Himpsel, and R. C. C. Perera, "Resonant inelastic x-ray scattering in hexagonal boron nitride observed by soft-x-ray fluorescence spectroscopy," Phys. Rev. Lett. **76**, 4054–4057 (1996).
[48]J. A. Carlisle, L. J. Terminello, E. A. Hudson, R. C. C. Perera, J. H. Underwood, T. A. Callcott, J. J. Jia, D. L. Ederer, F. J. Himpsel, and M. G. Samant, "Characterization of buried thin films with resonant soft x-ray fluorescence," Appl. Phys. Lett. **67**, 34–36 (1995).
[49]A. Nicolaou, K. Ruotsalainen, L. Susana, V. Porée, L. G. Tizei, J. Koskelo, T. Taniguchi, K. Watanabe, A. Zobelli, and M. Gatti, "Direct measurement of the longitudinal exciton dispersion in *h*-BN by resonant inelastic x-ray scattering," Phys. Rev. B **112**, 085207 (2025).
[50]J. Vinson, T. Jach, M. Müller, R. Unterumsberger, and B. Beckhoff, "Resonant x-ray emission of hexagonal boron nitride," Phys. Rev. B **96**, 205116 (2017).
[51]R. Decker, Y. Wang, V. W. Brar, W. Regan, H.-Z. Tsai, Q. Wu, W. Gannett, A. Zettl, and M. F. Crommie, "Local electronic properties of graphene on a BN substrate via scanning tunneling microscopy," Nano Lett. **11**, 2291–2295 (2011).
[52]J. Xue, J. Sanchez-Yamagishi, D. Bulmash, P. Jacquod, A. Deshpande, K. Watanabe, T. Taniguchi, P. Jarillo-Herrero, and B. J. LeRoy, "Scanning tunnelling microscopy and spectroscopy of ultra-flat graphene on hexagonal boron nitride," Nat. Mater. **10**, 282–285 (2011).
[53]J. B. MacNaughton, A. Moewes, R. G. Wilks, X. T. Zhou, T. K. Sham, T. Taniguchi, K. Watanabe, C. Y. Chan, W. J. Zhang, I. Bello, S. T. Lee, and H. Hofsäss, "Electronic structure of boron nitride single crystals and films," Phys. Rev. B **72**, 195113 (2005).
[54]A. W. Hahn, B. E. Van Kuiken, V. G. Chilkuri, N. Levin, E. Bill, T. Weyhermüller, A. Nicolaou, J. Miyawaki, Y. Harada, and S. DeBeer, "Probing the valence electronic structure of low-spin ferrous and ferric complexes using 2p3d resonant inelastic x-ray scattering (RIXS)," Inorg. Chem. **57**, 9515–9530 (2018).
[55]L.-C. Duda, J. Stöhr, D. C. Mancini, A. Nilsson, N. Wassdahl, J. Nordgren, and M. G. Samant, "Magnetic dichroism in $l_{2,3}$ emission of Fe, Co, and Ni following energy-dependent excitation with circularly polarized x rays," Phys. Rev. B **50**, 16758–16761 (1994).
[56]M. Sikora, A. Juhin, T.-C. Weng, P. Sainctavit, C. Detlefs, F. de Groot, and P. Glatzel, "Strong *k*-edge magnetic circular dichroism observed in photon-in–photon-out spectroscopy," Phys. Rev. Lett. **105**, 037202 (2010).
[57]D. B. Rice, D. Wong, T. Weyhermüller, F. Neese, and S. DeBeer, "The spin-forbidden transition in iron(IV)-oxo catalysts relevant to two-state reactivity," Sci. Adv. **10**, eado1603 (2024).
[58]J. A. Carlisle, E. L. Shirley, E. A. Hudson, L. J. Terminello, T. A. Callcott, J. J. Jia, D. L. Ederer, R. C. C. Perera, and F. J. Himpsel, "Probing the graphite band structure with resonant soft-x-ray fluorescence," Phys. Rev. Lett. **74**, 1234–1237 (1995).